Key Points:
- Average values of the real part of dry aerosol refractive index (n) varied between 1.50 and 1.53 for various air mass types
- A characteristic value of 1.52 is shown to apply to organic aerosol (n_{OA}) for the cumulative data set
- Values of n_{OA} were positively (negatively) correlated with the O:C (H:C) ratio in the absence of biomass burning

Supporting Information:
- Supporting Information S1

Correspondence to:
A. Sorooshian,
armin@email.arizona.edu

Characterization of the Real Part of Dry Aerosol Refractive Index Over North America From the Surface to 12 km

Abdulmonam M. Aldhaif[1] (iD), Connor Stahl[1], Rachel A. Braun[1] (iD), Mohammad A. Moghaddam[2], Taylor Shingler[3,4], Ewan Crosbie[3,4] (iD), Patricia Sawamura[3,4], Hossein Dadashazar[1] (iD), Luke Ziemba[4] (iD), Jose L. Jimenez[5,6] (iD), Pedro Campuzano-Jost[5,6] (iD), and Armin Sorooshian[1,2] (iD)

[1]Department of Chemical and Environmental Engineering, University of Arizona, Tucson, AZ, USA, [2]Department of Hydrology and Atmospheric Sciences, University of Arizona, Tucson, AZ, USA, [3]Science Systems and Applications, Inc., Hampton, VA, USA, [4]NASA Langley Research Center, Hampton, VA, USA, [5]Cooperative Institute for Research in Environmental Sciences, University of Colorado, Boulder, CO, USA, [6]Department of Chemistry and Biochemistry, University of Colorado, Boulder, CO, USA

Abstract This study reports a characterization of the real part of dry particle refractive index (n) at 532 nm based on airborne measurements over the United States, Canada, the Pacific Ocean, and the Gulf of Mexico from the 2012 Deep Convective Clouds and Chemistry (DC3) and 2013 Studies of Emissions and Atmospheric Composition, Clouds and Climate Coupling by Regional Surveys (SEAC4RS) campaigns. Effective n values are reported, with the limitations and uncertainties discussed. Eight air mass types were identified based on criteria related to gas-phase tracer concentrations, location, and altitude. Average values of n for these air types ranged from 1.50 to 1.53. Values of n for the organic aerosol (OA) fraction (n_{OA}) were calculated using a linear mixing rule for each air mass type, with 1.52 shown to be a good approximation for all OA. Case studies detailing vertical structure revealed that n and n_{OA} increased with altitude, simultaneous with enhancements in the mass fraction of OA. Values of n_{OA} were positively (negatively) correlated with the O:C (H:C) ratio in the absence of biomass burning influence; in contrast, the cumulative data set revealed a slight decrease in n_{OA} as a function of the O:C ratio. The performance of parametric (multiple linear regression) and nonparametric (Gaussian process regression) methods in predicting n based on aerosol composition data is discussed. It is shown that even small perturbations in n values significantly impact aerosol optical depth retrievals, radiative forcing, and optical sizing instruments, emphasizing the importance of further improving the understanding of this important aerosol property.

1. Introduction

The refractive index (m) of atmospheric aerosol particles is a critical optical property that is used both in calculating parameters relevant to radiative transfer (e.g., extinction coefficient, single scattering albedo, and asymmetry factor) and for quantitative interpretation of data from optically based measurement devices such as optical particle counters (OPCs). There are two parts associated with the complex m of aerosol particles ($m = n - ik$), including the real (n) and imaginary (k) components, which account for scattering and absorption, respectively. Poorly constrained values of m, especially for organic compounds (Cappa et al., 2011; Zarzana et al., 2014) as compared to inorganics (Abo Riziq et al., 2007), contribute to one of the largest sources of uncertainty in estimating aerosol effects on climate and total radiative forcing (Intergovernmental Panel on Climate Change, 2013). Furthermore, m is a necessary parameter in atmospheric models to compute optical properties (e.g., Chin et al., 2002; Kaufman et al., 1997; Kinne et al., 2003). Models obtain optical property data from lookup tables such as in the Global Aerosol Data Set (Koepke et al., 1997).

The focus of this work is the real component of dry particle refractive indices (n). The aforementioned applications and impacts of n typically apply to ambient particles that have undergone some amount of humidification. Therefore, it is important to note that the n value of dry particles are typically converted to the corresponding value for humidified particles using a volume-weighted mixing rule approach using the refractive index of water (e.g., Levoni et al., 1997; Shettle & Fenn, 1979). Past measurement studies of ambient aerosol particles have reported a wide range of n values, usually between 1.4 and 1.6, with variability attributed to instrument wavelength, dry particle size, air mass type, and composition (e.g., Dubovik et al., 2002; Ferrare et al., 1998; Guyon et al., 2003; Wang & Rood, 2008). There is a limited inventory of vertically resolved n data

(e.g., Raut & Chazette, 2008), which is needed to quantify aerosol effects on vertical temperature profiles, convection and redistribution of pollutants, and large-scale circulation patterns. In the absence of a direct measurement, it is helpful to predict n based on other properties of aerosol. There is a scarcity of closure studies that attempt to quantify the level of agreement between measured and predicted n values for ambient aerosol. Poor skill in predicting n values is problematic because a small error (5% change) can translate to a change of ~30% in the radiative flux change at the top of the atmosphere (Redemann, Turco, Liou, Hobbs, et al., 2000). An AERONET-based study showed that n values were the largest source of uncertainty in modeled aerosol composition and aerosol water volume fraction (van Beelen et al., 2014).

The goal of this work is to report a characterization of n over North America using a combined data set collected from two separate field campaigns in successive years (2012 and 2013). Owing to the extensive payload of instruments used during the campaigns, it was possible to (i) define eight different air mass types, (ii) categorize n values as a function of air mass type and altitude, (iii) derive values of n associated with organic aerosol (n_{OA}) and examine their relationship with the oxygen-to-carbon (O:C) atomic ratio of organic aerosol (OA), (iv) use case studies in different areas of North America to investigate spatial variability in n and how it is related to aerosol composition, including an examination of how well linear and nonlinear models can predict n based on aerosol composition data, and (v) to put results of this work into perspective with calculations of how both aerosol optical depth (AOD) and radiative forcing are sensitive to n perturbations.

2. Experimental Methods

2.1. Field Campaign Descriptions

Data used in this study were taken over the continental United States, southern parts of Canada, the northeastern Pacific Ocean, and the Gulf of Mexico during two field campaigns using the NASA DC-8 aircraft (flight tracks shown in Figure 1). The first campaign was the Deep Convective Clouds and Chemistry (DC3) campaign based in Salina, Kansas in May–June 2012 (Barth et al., 2015). DC3 was a multiplatform campaign aimed at studying the chemical and transport processes associated with deep convection, with a focus on storms developing over Alabama, Colorado, North Texas, and Oklahoma. DC3 consisted of four test flights and 18 research flights. The second campaign was the Studies of Emissions and Atmospheric Composition, Clouds and Climate Coupling by Regional Surveys (SEAC[4]RS) based out of Houston, Texas in August–September 2013 (Toon et al., 2016). SEAC[4]RS was a multiplatform effort focused on the atmospheric composition over North America, with two test flights and 21 research flights conducted with the DC-8.

Because of the wide spatial range of the flights, numerous aerosol types, based on criteria in Table 1 (adopted from Shingler, Crosbie, et al., 2016), were sampled during the campaigns. A total of 19,303 data points were resolved into the following categories (number of points, N; cumulative sample time): Biomass Burning (BB)-Agricultural (150; 0.34 hr), Background (7,472; 37.75 hr), BB-Wildfire (2,599; 8.18 hr), Biogenic (5,234; 22.19 hr), Free Troposphere (FT; 1,981; 23.99 hr), Marine (500; 3.52 hr), Urban (407; 1.78 hr), and Mix (960; 2.79 hr).

2.2. Instrument Data Sets

2.2.1. DASH-SP Description

The Differential Aerosol Sizing and Hygroscopicity Spectrometer Probe (DASH-SP) provided rapid measurements of size-resolved dry particle n values during both DC3 and SEAC[4]RS. The instrument has been discussed extensively in previous work, with most of the scientific focus placed on data derived for hygroscopic growth factors, representing the ratio of humidified particle diameter to dry diameter (Hersey et al., 2009, 2011, 2013; Shingler, Crosbie, et al., 2016; Shingler, Sorooshian, et al., 2016; Sorooshian, Hersey, et al., 2008; Sorooshian, Murphy, et al., 2008; Sorooshian et al., 2017). Sampled particles first pass through an isokinetically controlled inlet (McNaughton et al., 2007) prior to going through a dryer at the inlet of the DASH-SP. Dried particles subsequently pass through an aerosol charge neutralizer and a classification differential mobility analyzer that produces a stream of dry, monodisperse particles. Those particles are then split into two streams and fed to separate OPCs measuring light scattering with diode lasers at a wavelength of 532 nm (World Star Technologies, Model TECGL-30). One stream keeps particles in a dry state while the other includes a diffusion-based aerosol conditioning module to bring particles to equilibrium at a controlled and enhanced relative humidity (RH) prior to the OPC measurement. During the DC3 and SEAC[4]RS campaigns, the DASH-SP sampled particles with scanning between dry diameters ($D_{p,dry}$) between 180 and 400 nm. The RH in the dry OPC sampling channel was usually maintained below 15% (mean ± standard
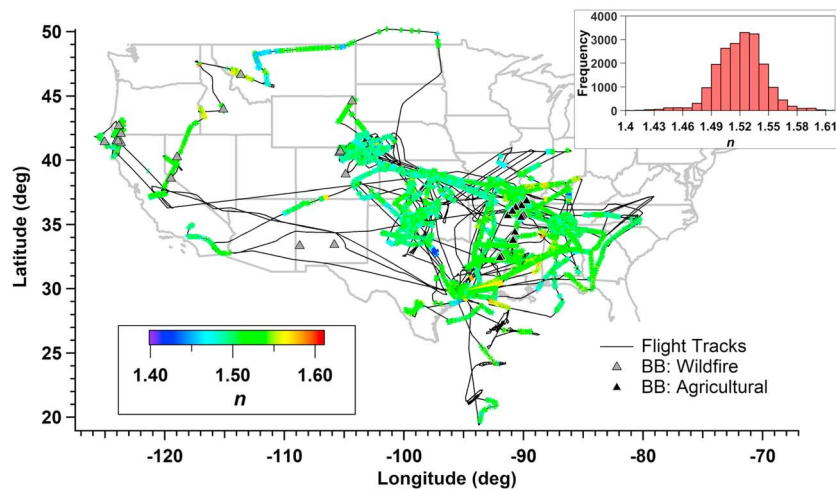
Figure 1. Spatial map of DC-8 flights (black trace) during Deep Convective Clouds and Chemistry (4 test, 18 research) and Studies of Emissions and Atmospheric Composition, Clouds and Climate Coupling by Regional Surveys (2 test, 21 research). Colored markers represent measured DASH-SP n values. Locations are shown for biomass burning (BB) events from wildfires and agriculture. The inset histogram shows the frequency of occurrence of different n values in 0.01 increments.

deviation = 12% ± 4%), which is the channel from which the dry particle n data are derived. Note that the wet aerosol n values from the humidified OPC channel data are not used in this study as they are not representative of ambient RH but rather a prescribed instrument RH.

Values of n are calculated from a calibration surface developed by determining the OPC electrical pulse height signals for 36 dry mobility size settings between 150 and 500 nm for various calibration salts with known n values (i.e., LiF, Na$_2$SO4, K$_2$SO4, (NH$_4$)$_2$SO4, NaCl, and polystyrene latex spheres). More specifically, Figure S1 in the supporting information shows a representative calibration surface for $D_{p,dry}$ versus electrical pulse height, with different colored markers for salts of varying n values. High-order polynomial equations are derived based on the markers for each individual salt such that n can be determined based on knowledge of $D_{p,dry}$ and electrical pulse height. The uncertainty (or error), taken as the standard deviation (e.g., Taylor, 1982), in the n measurement varies based on where a sampled particle resides in $D_{p,dry}$-pulse height space. Figure S1 and Table S1 summarize the uncertainty and also the precision, considered to be fractional uncertainty (Taylor, 1982), associated with the DASH-SP as a function of $D_{p,dry}$ and n. Of note is that there is a clear separation between data for different salts at a fixed $D_{p,dry}$ with the average precision being between 1% and 3% based on the salt across the entire range of $D_{p,dry}$ values tested. A representative uncertainty of 0.006 was derived for n based on Table S1 by (i) averaging the fractional uncertainty across all $D_{p,dry}$ values for individual salts, (ii) taking an average of the overall fractional uncertainty for the six salts, and (iii) multiplying the latter

Table 1
Criteria Used for Defining Different Air Mass Types Based on the Work of Shingler, Crosbie, et al. (2016)

Air mass type	Criteria
BB-Wildfire	Acetonitrile > 250 pptv or (when acetonitrile unavailable) CO > 250 ppbv in nonurban areas
BB-Agricultural	Same as BB-Wildfire with additional visual confirmation of crop burning
Biogenic	Isoprene + monoterpenes + MVK + MACR > 2 ppbv and acetonitrile < 250 pptv
Marine	In PBL; over ocean and greater than 40 km from the coast
Urban	In PBL; spatially over Houston (30.50°N, −94.60°W to 29.00°N, −96.10°W) or Los Angeles (34.17°N, −117.00°W to 33.44°N, −119.75°W)
Background	In PBL; did not fit into first five categories
Free Troposphere (FT)	Above PBL; did not fit into first five categories
Mix	Fit into more than one of the first five categories

Note. BB = biomass burning, PBL = planetary boundary layer.

result by the average n value for the six salts tested. This provides confidence in distinguishing between n differences of 0.01 between the lower and upper limits of n reported in this study (1.42 and 1.61, respectively).

It is important to clarify that the n values retrieved by the DASH-SP should not be considered as true values but rather effective values as this single parameter incorporates the roles of shape and absorbing materials. Such a designation is often made for optically based instruments (e.g., Rosati et al., 2015; Shingler, Crosbie, et al., 2016). The DASH-SP algorithm assumes that particles are spherical; however, during calibrations, the cubic nature of NaCl is accounted for by using a dynamic shape factor of 1.08 (Hameri et al., 2001). Aerosol with a significant imaginary component k can impact the OPC scattering signal (e.g., Shingler, Crosbie, et al., 2016). More specifically, absorbing components can lead to an underestimate of n. Black carbon (BC) comprised a small fraction of the overall particle composition in DC3 and SEAC[4]RS (mass fraction $\leq$ 2%; Perring et al., 2017; Shingler, Crosbie, et al., 2016; Sorooshian et al., 2017). Furthermore, mean single scattering albedo (SSA) values at 550 nm, as derived from the Langley Aerosol Research Group Experiment package described below, were within the range of values expected for aged particles without strong absorptive properties (0.91–0.99) as compared to fresh wildfire emissions (e.g., Corr et al., 2012): DC3 = 0.93 ± 0.04, SEAC[4]RS = 0.95 ± 0.02.

2.2.2. Other Instrumentation

Data from a number of other instruments were time synchronized with the DASH-SP. As part of the criteria used for air mass categorization, gas-phase data were used from the proton transfer reaction-mass spectrometer (de Gouw & Warneke, 2007) for selected species, including methacrolein, methyl vinyl ketone, monoterpenes, isoprene, and acetonitrile. Carbon monoxide data were obtained with a folded-path, differential absorption mid-IR diode laser spectrometer (Sachse et al., 1987). Nonrefractory composition for submicrometer particles, including oxygen-to-carbon (O:C) and hydrogen-to-carbon (H:C) atomic ratios, was measured with an Aerodyne high-resolution time-of-flight aerosol mass spectrometer (Canagaratna et al., 2007; DeCarlo et al., 2006). BC data were obtained with a humidified-dual single-particle soot photometer (Schwarz et al., 2015). To assist with identifying the height of the planetary boundary layer, water vapor data are used from the diode laser hygrometer (Diskin et al., 2002). Aerosol data were used from the Langley Aerosol Research Group Experiment instrument package for both single scattering albedo (at 550 nm), as measured by a TSI 3563 integrating nephelometer, and aerosol size distributions between diameters of 60 nm and 1 μm using an ultra-high sensitivity aerosol spectrometer (Droplet Measurement Technologies, Inc.).

2.3. Modeling

To investigate the n-composition relationships in more depth, linear and nonlinear regression techniques were used. The first modeling method was multiple linear regression (MLR) analysis, which describes the dependence of a response on several independent variables:

$$\widehat{y}_i = \beta_1 + \beta_2 x_2 + \dots + \beta_n x_n \qquad (1)$$

where $\widehat{y}_i$, β_1, and β_n are the predicted response (i.e., n in this study), the intercept, and the regression coefficient of the predictor variables (i.e., x_i), respectively.

In the second modeling approach, Gaussian process regression (GPR) was utilized to evaluate the performance of a nonlinear technique for prediction of n. GPR is a convenient and powerful regression nonparametric approach used in a diversity of fields ranging from biology to Earth sciences and chemical engineering (e.g., Reggente et al., 2015; Wang et al., 2017). Unlike parametric approaches such as MLR, GPR is a probabilistic modeling approach with the ability to predict uncertainty of estimations (Rogers & Girolami, 2016). Assuming a relationship of the form $n_i = f(x_i) + \varepsilon$ between the predictors, x_i, the response value, n_i, and error term, $\varepsilon_n = \mathcal{N}(0, \sigma^2)$, GPR generates a joint multivariate Gaussian distribution over vectors of responses with the mean of μ^* and covariance matrix of Σ^*. To obtain Σ^*, we employed the rational quadratic kernel (RQK), expressed as follows:

$$c(x_i, x_j) = \sigma^2 \left(1 + \frac{r^2}{2\alpha\sigma_l^2}\right)^{-\alpha} \qquad (2)$$

RQK is derived as a scale mixture of squared exponential kernels of different length scales (Wilson & Adams, 2013), in which α is scale-mixture parameter, r is the Euclidean distance between x_i and x_j, and σ_l is the

characteristic length scale that determines how fast the Gaussian Process function varies with the provided input. The distribution of predicted values, f^*, relies on σ^2 and the observation values at the training points, n_i. The predictive conditional distribution $p(f^*|n, \sigma^2)$ is expressed as follows (Rogers & Girolami, 2016):

$$p\left(f^*|n,\sigma^2\right) = \mathcal{N}(\mu^*, \Sigma^*) \tag{3}$$

where

$$\mu^* = R^{\mathrm{T}}\left(C + \sigma^2 I_N\right)^{-1} n \tag{4}$$

$$\Sigma^* = C^* - R^{\mathrm{T}}\left(C + \sigma^2 I_N\right)^{-1} R \tag{5}$$

and I is the identity matrix with size of $N \times N$, with N being the number of training sets and C being the covariance matrix for the training sets:

$$C = \begin{bmatrix} c(x_1, x_1) & \dots & c(x_1, x_N) \\ \vdots & \dots & \vdots \\ c(x_N, x_1) & \dots & c(x_N, x_N) \end{bmatrix} \tag{6}$$

C^* is the covariance matrix with size of $L \times L$, where L is the number of testing data points for the testing set:

$$C^* = \begin{bmatrix} c\left(x_1^*, x_1^*\right) & \dots & c\left(x_1^*, x_L^*\right) \\ \vdots & \dots & \vdots \\ c\left(x_L^*, x_1^*\right) & \dots & c\left(x_L^*, x_L^*\right) \end{bmatrix} \tag{7}$$

Finally, R is a $N \times L$ cross-covariance matrix, which evaluates the similarity between features of training and testing points.

$$R = \begin{bmatrix} c\left(x_1, x_1^*\right) & \dots & c\left(x_1, x_L^*\right) \\ \vdots & \dots & \vdots \\ c\left(x_N, x_1^*\right) & \dots & c\left(x_N, x_L^*\right) \end{bmatrix} \tag{8}$$

The GPR RQK analysis was conducted using the Regression Learner application in MATLAB, with the addition of k-fold cross validation ($k = 5$). This involved dividing the original data set randomly into five subsamples, with one considered as the testing set for validating the model trained by the other four sets. This process was repeated a total of five times with the results averaged at the end.

3. Results and Discussion

3.1. Cumulative Data

3.1.1. Air Mass Type Categorization of n

A spatial map of n values from DC3 and SEAC^{4}RS is shown in Figure 1, while Table S2 reports descriptive statistics for each air mass type that are also visually summarized in Figure 2 in the form of a box-and-whisker plot. The results reveal that although a wide range was observed (1.42–1.61), most n values were within a narrower range, regardless of location and air mass type. The average and median n values for each air mass type varied between 1.50–1.53 and 1.50–1.54, respectively. The Urban and BB-Wildfire air types exhibited the highest median (1.54), while the FT air type exhibited the lowest median (1.50). The interquartile range was narrowest for BB-Agricultural (0.01), with the widest range (0.03) for four other air types (Background, FT, Marine, and Urban). The overall range of values was narrowest for the BB-Agricultural (0.08) category and widest for the Biogenic and FT categories (0.19). There is a significant variability within a single air mass type, which has implications for assuming a fixed value. As noted already, a 5% change in n can yield a ~30% change in the radiative flux at the top of the atmosphere (Redemann, Turco, Liou, Hobbs, et al., 2000).

There are scarce reports of vertically resolved n values, especially as a function of air mass type. The results of the limited reports from the literature reveal that there exist vertical layers with distinct n values (Ferrare et al.,
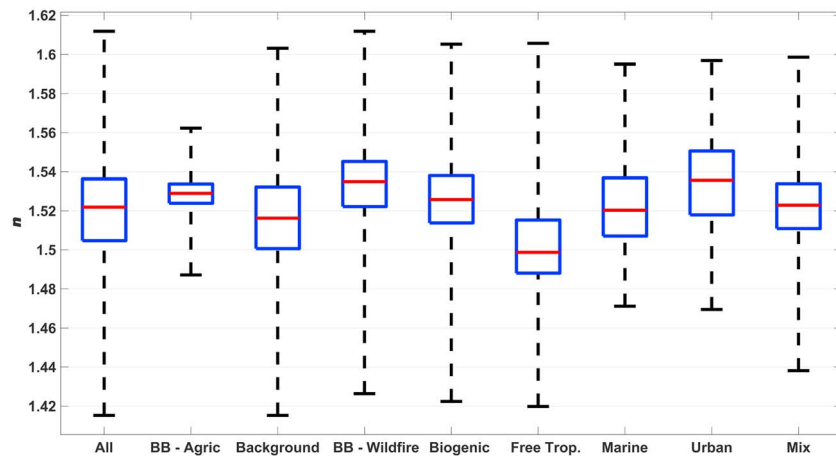
Figure 2. Box-and-whisker summary of *n* values for each air mass type sampled during both Deep Convective Clouds and Chemistry and Studies of Emissions and Atmospheric Composition, Clouds and Climate Coupling by Regional Surveys. The lower (Q1) and upper quartile (Q3) are represented as the bottom and top bounds of the boxes, respectively, with the ends of the lines representing the minimum and maximum values. Numbers of points in each category are as follows: All = 19,303, Biomass Burning (BB)-Agricultural = 150, Background = 7,472, BB-Wildfire = 2,599, Biogenic = 5,234, Free Troposphere = 1,981, Marine = 500, Urban = 407, and Mix = 960.

1998; Redemann, Turco, Liou, Russell, et al., 2000). Knowledge of *n* variability with altitude is important for whether assumptions of a constant columnar value are valid. Vertically resolved values of *n* are reported for each air mass type in Figure 3. There is inhomogeneity in *n* values as a function of altitude within an air mass type and especially high variability in the BB-Wildfire category. A series of case studies are subsequently analyzed to examine the degree of vertical variability in fixed areas without mixing data from numerous flights such as in Figure 3.

Table 2 reports values from other regions to place the values in this work in context. For those studies with *n* data at the same wavelength as this study (532 nm), *n* values were similar. The ranges of values for BB-Agricultural (1.49–1.56) and BB-Wildfire (1.43–1.61) were mostly in the range of those used in models and calculations for biomass burning smoke aerosol (1.47–1.58) (Anderson et al., 1996; Dubovik et al., 2002; Lenoble, 1991; Westphal & Toon, 1991).

3.1.2. Application of the Linear Mixing Rule

While *n* values of pure species such as inorganic salts (NaCl, $(NH_4)_2SO_4$) are well established, those for carbonaceous species are less certain, especially since values for OA species depend on precursor type, oxidation pathway for formation, and aging of secondary organic aerosol (SOA) and particle growth (Cappa et al., 2011; Flores et al., 2014; Kim et al., 2010, 2012; Kim & Paulson, 2013; Moise et al., 2015). In their review paper, Moise
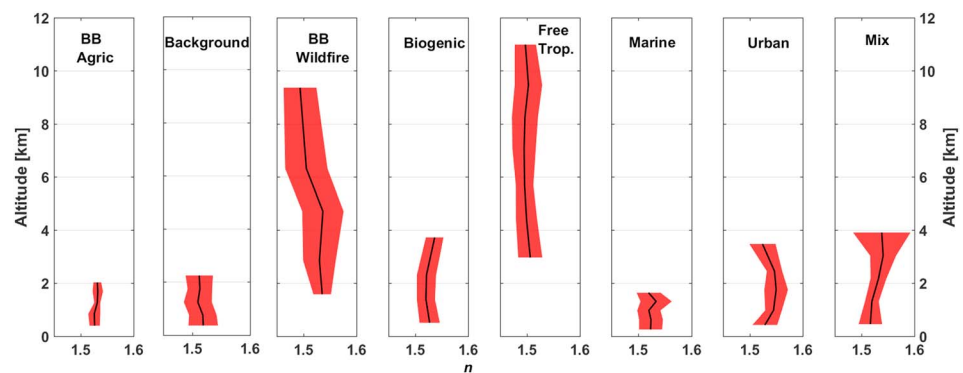

Figure 3. Vertical profile of *n* for dry aerosol sampled during both Deep Convective Clouds and Chemistry and Studies of Emissions and Atmospheric Composition, Clouds and Climate Coupling by Regional Surveys as a function of air mass type. Black lines represent averages, and borders of the red shading represent one standard deviation. BB = biomass burning.

Table 2
Values of the Real Part of Dry Aerosol Refractive Index (n) Reported for Other Regions

Region	n (wavelength)	Reference
United States Eastern Seaboard	1.33–1.45 (815 nm)	Redemann, Turco, Liou, Russell, et al. (2000)
Big Bend National Park (southwest Texas)	1.566 ± 0.12 (632.8 nm)	Hand and Kreidenweis (2002)
Southern Great Plains ARM site (Oklahoma)	1.4–1.5 (351, 530, and 1,069 nm)	Ferrare et al. (1998)
Cuiaba, Brazil (smoke influence)	1.53–1.59 (438–1,020 nm)	Yamasoe et al. (1998)
Beijing, China	1.50–1.53 (532 nm)	Li and Mao (1990)
Paris, France	1.51 ± 0.02 (532 nm)	Raut and Chazette (2008)
European plumes over Atlantic Ocean	1.56 ± 0.07 (532 nm); range: 1.45–1.67	Muller et al. (2002)
Bovine source in California	1.48–1.51 (532 nm)	Sorooshian, Murphy, et al. (2008)
Northwest China	1.47–1.55 (400, 500, 675, 870, and 1,220 nm)	Liu et al. (2008)

et al. (2015) showed that n for SOA ranges from 1.35 to 1.6. Here we use the field data set to derive values for n_{OA} to then compare to other reported values in the literature, which are mostly from controlled laboratory experiments.

Perhaps the simplest way to predict n for multicomponent particles is a linear average of n values of each pure component weighted by its respective volume fraction, as shown in equation (9) (e.g., Redmond & Thompson, 2011; Seinfeld & Pandis, 2016; Sokolik & Toon, 1999):

$$n = \Sigma \phi_i n_i \qquad (9)$$

where ϕ_i represents the volume fraction of each component i. Individual volume fractions are calculated as follows using knowledge of the mass concentration and density of each species considered:

$$\phi_i = \frac{\frac{m_i}{\rho_i}}{\Sigma \frac{m_i}{\rho_i}} \qquad (10)$$

This sort of volume-weighted mixing rule, which is empirical in nature, is applied in general circulation models to quantify radiative forcing of internally mixed aerosols (e.g., Haywood et al., 1997; Myhre et al., 1998). This approach assumes that particles are uniformly internally mixed. In contrast to other mixing rules (e.g., Maxwell-Garnett rule, extended effective medium approximation), a simple linear mixing rule was shown to be the best predictor of n for non-absorbing materials in past work relying on cavity ring-down spectroscopy (Abo Riziq et al., 2007). That work also showed that for aerosol with a small volume fraction of absorbing substances, all mixing rules yielded similar results.

Using volume fractions relies on assumptions about both density and n values for individual aerosol constituents. Representative values used in past work are summarized in Table 3. One of the largest uncertainties in Table 3 is the n value associated with OA. Rather than use a volume-weighted mixing rule to derive a predicted n value, an alternative approach applied here is to use the measured n value in Equation (9) to back-calculate a value for n_{OA}. The current data set allows for such an investigation with the cautionary note that only bulk aerosol composition data for submicrometer aerosol are used. While

Table 3
Values of n and Density (ρ) Assigned to Various Aerosol Constituents in Past Studies

Constituent	n	Reference	ρ (g/cm^3)	Reference
Black Carbon	1.960	Hand and Kreidenweis (2002)	2.000	Hand and Kreidenweis (2002)
Organic aerosol	1.550	Zhang et al. (1994) and Hand and Kreidenweis (2002)	1.400	Dick et al. (2000) and Hand and Kreidenweis (2002), and Gysel et al. (2007)
$(NH_4)_2SO_4$	1.530	Zhang et al. (1994), Tang (1996), and Hand and Kreidenweis (2002)	1.769	Gysel et al. (2007)
NH_4HSO_4	1.473	Tang (1996)	1.780	Tang (1996) and Gysel et al. (2007)
H_2SO_4	1.408	Hand and Kreidenweis (2002)	1.830	Gysel et al. (2007)
NH_4NO_3	1.554	Tang (1996)	1.720	Gysel et al. (2007)

size-resolved composition data were collected, the signal-to-noise ratio for this particular data set is too limited to inform our analyses. However, the averaged size distributions suggest internally mixed aerosol, except in fresh biogenic plumes. Lastly, this analysis assumes all non-OA species not shown in Table 3 are consumed in the value of n_{OA}.

An ion pairing technique (e.g., Gysel et al., 2007) was used to obtain values for volume fractions for inorganic constituents (ammonium nitrate, sulfuric acid, ammonium bisulfate, and ammonium sulfate) using data from the high-resolution time-of-flight aerosol mass spectrometer. Additionally, OA and BC constituted two separate categories. Data for densities and n values for pure aerosol constituents from Table 3 were applied to equations (9) and (10) with the exception of n_{OA}. Additionally, OA density was calculated using the following formula (Kuwata et al., 2012):

$$\rho_{OA} = 1,000 \frac{[12 + 1(H:C) + 16(O:C)]}{[7 + 5(H:C) + 4.15(O:C)]} \tag{11}$$

Table 4 shows that the value of n_{OA} is 1.52 ± 0.03 for the cumulative data set, with a mean value varying between 1.50 and 1.59 for individual air mass types. With the exception of the Marine category, which exhibited a relatively smaller sample set ($N = 200$) and exhibited high variability (standard deviation = 0.04), values for the other air mass types and the cumulative data set were less than the 1.55 value reported in Table 3 in past work. To put the n_{OA} values from Table 4 in more context, the range of n values for SOA (1.35–1.60) reported in the review study by Moise et al. (2015) encompasses the mean and median values derived in this work for n_{OA}. Controlled experiments have provided values for biogenic SOA (1.44) and anthropogenic SOA (1.55) at 532 nm (Kim & Paulson, 2013), which is consistent with how the mean n_{OA} for the Urban air type (1.54) exceeded that of the Biogenic type (1.52). Redmond and Thompson (2011) reported n values of 1.49–1.51 and 1.49–1.50 at 532 nm for SOA generated from α-pinene and toluene, respectively.

The oxygen-to-carbon (O:C) atomic ratio of OA is often used as a proxy for oxidation state of OA, where conflicting results exist in the literature with n both decreasing and increasing as a function of O:C ratio for various organic systems (Moise et al., 2015). For example, He et al. (2018) observed an increase followed by a reduction in n_{OA} as a function of the O:C ratio for SOA derived from precursors such as p-xylene and β-pinene. In contrast, Cappa et al. (2011) showed that n increased with oxidation lifetime for squalene (proxy for primary OA) and azelaic acid (proxy for oxidized OA) from 1.49 to 1.54 and 1.48 to 1.55, respectively. The relationship between n_{OA} and the O:C ratio for the cumulative data set is summarized in Figure 4. Data from the Moise et al. (2015) review study are also shown to demonstrate that the variability observed in the atmosphere during DC3 and SEAC⁴RS was similar to that observed in SOA laboratory studies. Owing to considerable scatter, the O:C data were also represented as decile averages to illuminate potential hidden trends. Owing to the lack of strong dependence of n_{OA} on the O:C ratio, a value of 1.52 is suggested here as a good approximation for n_{OA}. While not a strong feature, an interesting aspect of the decile average representation in Figure 4 is that there is slight decreasing trend in n_{OA} above an O:C ratio of 0.60. Others have also observed decreases in n_{OA} as a function of the O:C ratio in

Table 4
A Summary of n_{OA} Values Retrieved Using the Linear Mixing Rule as a Function of Air Mass Type for the Cumulative Data Set

|	All	BB-Agric	Background	BB-Wildfire	Biogenic	Free trop.	Marine	Urban	Mix
Mean	1.52	1.52	1.51	1.53	1.52	1.50	1.59	1.54	1.52
St. dev.	0.03	0.01	0.03	0.03	0.02	0.03	0.04	0.03	0.02
Maximum	1.66	1.56	1.66	1.61	1.65	1.65	1.66	1.65	1.65
Minimum	1.39	1.43	1.40	1.41	1.41	1.39	1.47	1.47	1.44
Third quartile (75th percentile)	1.53	1.53	1.53	1.54	1.54	1.52	1.62	1.55	1.53
Median (50th percentile)	1.52	1.52	1.51	1.53	1.52	1.50	1.59	1.54	1.52
First quartile (25th percentile)	1.50	1.52	1.49	1.51	1.51	1.48	1.56	1.52	1.51
Count	16,689	118	6,427	2,201	4,905	1,938	200	225	675

Note. BB = biomass burning.
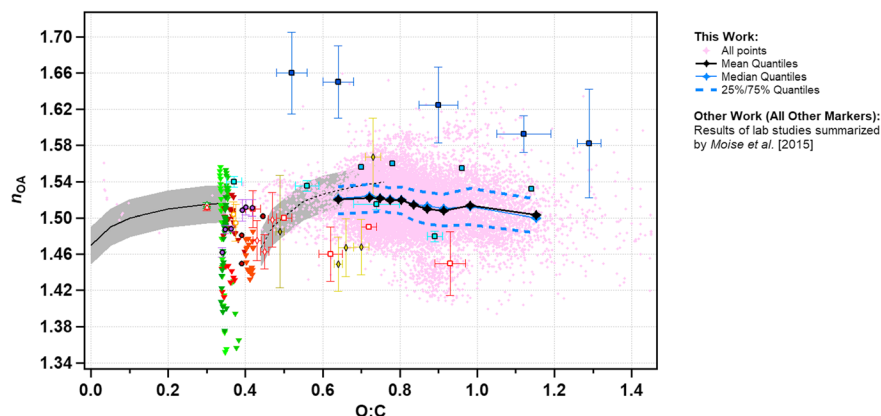
Figure 4. Relationship between n_{OA} and the O:C ratio of the organic aerosol fraction of the aerosol for the cumulative data set. The standard error on the mean quantile points is too small to see. Also shown are data for various secondary organic aerosol systems from Figure 8 of the review study of Moise et al. (2015).

the same general O:C range for OA derived from precursors such as naphthalene and tricyclo[5.2.1.0^{2,6}] decane (Lambe et al., 2013).

An uncertainty analysis analogous to that of Mei et al. (2013) for the derivation of organic hygroscopicity was conducted here for the derivation of n_{OA} to quantify the contributions to total uncertainty from values of n and volume fractions of participating species. Refer to the supporting information for the derivation of the equations used to summarize the uncertainty results in Figure S2. The uncertainty in the derivation of n_{OA} using the mixing rule decreased rapidly with increasing volume fraction of OA. As the mean and median of mass fraction (MF) of OA (MF_{OA}) were 0.63 and 0.65, respectively, for the cumulative data set, this points to reduced uncertainty in the derived n_{OA} values in this study. Since the uncertainty in n_{OA} values decreased as a function of contributions by OA using the linear mixing rule, it was of interest to examine the same relationship from Figure 4 when data were filtered for $MF_{OA} > 0.60$ (~40% of valid points; Figure S3) and $MF_{OA} > 0.80$ (~10% of valid points; Figure S4). The key characteristic from Figure 4 still preserved in Figures S3 and S4 is that an approximate value of 1.52 (mean value for "All" in Table 5) for n_{OA} is robust and that the relationships in Figures 4 and S3–S4 are intrinsic to OA and not caused by other uncertainties feeding in through the mixing rule.

As shown in the review study of Moise et al. (2015), the trend in n_{OA} with O:C could vary with source as revealed by results from various laboratory studies of biogenic and anthropogenic SOA. To examine this in greater detail with the field data set, a number of case studies are examined in the next section to determine what the dependence is of n_{OA} on both the O:C and H:C ratios of OA, with the latter being higher for less oxidized aerosols (including primary aerosols).

3.2. Case Studies

A series of case studies are examined here that exhibited significant correlations between n and composition, using the MF_{OA} as a representative proxy for composition. For each case study, the spatial variability of n and n_{OA} is reported, in addition to how n_{OA} is related to the two chemical ratios (O:C and H:C) representative of the OA fraction of aerosols. Lastly, the skill of parametric and nonparametric modeling approaches in predicting n using chemical data is assessed. While several case studies are noted below as having characterized vertical structure, there was still a horizontal variability owing to the aircraft often conducting slant soundings.
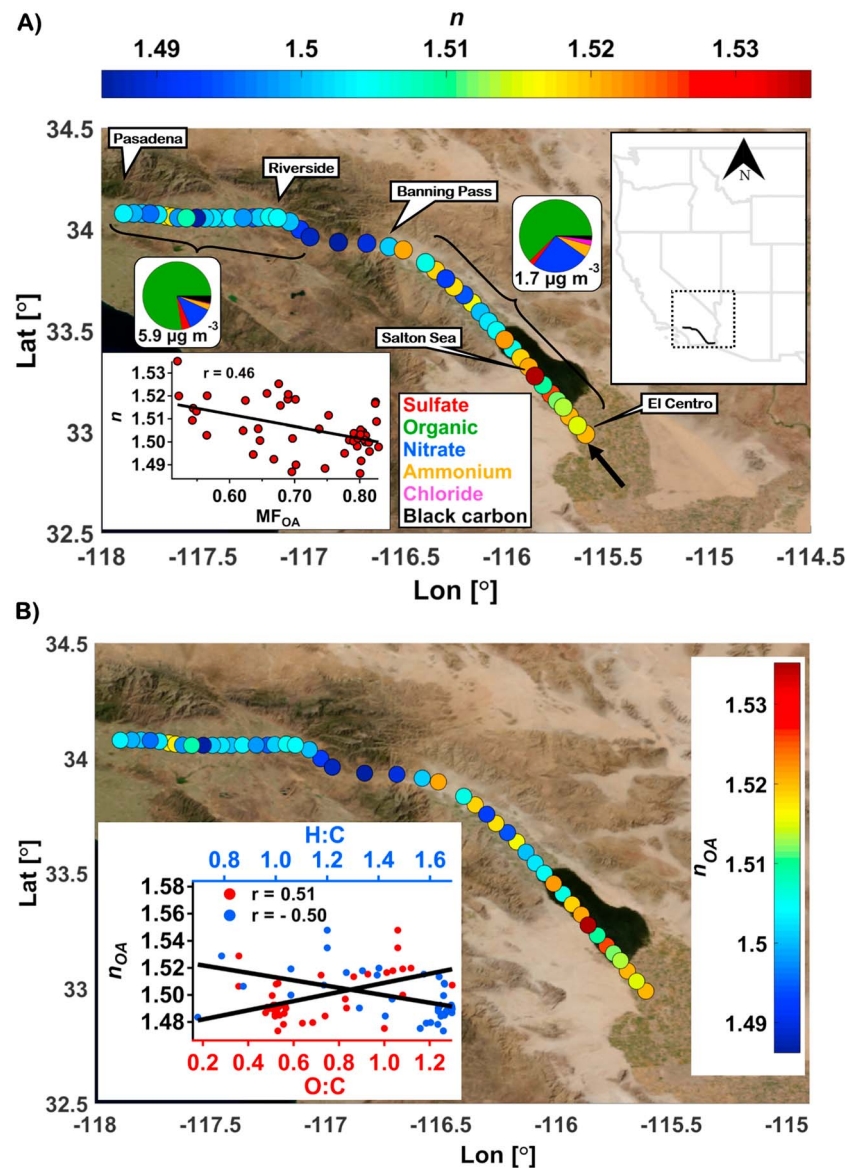
Table 5

Summary of Model Performance Based on Adjusted R^2 Values Using Gaussian Process Regression Rational Quadratics Kernel (GPR RQK) and Multiple Linear Regression (MLR) to Predict n with the Following Chemical Parameters: MF_{OA}, $MF_{nitrate}$, $MF_{sulfate}$, $MF_{ammonium}$, $MF_{chloride}$, MF_{BC}, and the O:C and H:C ratios of Organic Aerosol

Case	MLR	GPR RQK
Cumulative data set (Figures 1–3)	0.21	0.61
S. California (Figure 5)	0.16	−0.04
Fort Worth (Figure 6)	0.64	0.48
Houston (Figure 7)	0.54	0.58
Wyoming 1 (Figure 8)	0.72	0.71
Wyoming 2 (Figure 9)	0.45	0.48
Kansas (Figure 10)	0.96	0.80

Note. Note that a negative R^2 value for GPR RQK means that the trained model performs more poorly than the model where the response is constant and equals the mean of the training response. MF = mass fraction.

Figure 5. Transect during a Studies of Emissions and Atmospheric Composition, Clouds and Climate Coupling by Regional Surveys flight on 23 September 2013 (16:08–16:41 local time) across southern California showing (a) variability in n at relatively fixed altitude (0.34 ± 0.04 km) and $D_{p,dry}$ (195 nm). The two major air mass types sampled for the majority of the sounding were Background and Urban. The arrow signifies the direction of aircraft movement. The inset plot shows the relationship between n and mass fraction of organic aerosol (MF$_{OA}$). (b) Same as (a) but for n_{OA} and with the inset plot showing how n_{OA} depends on the O:C and H:C ratios of organic aerosol.

3.2.1. Boundary Layer Variability Across Southern California

A unique opportunity presented itself during the 23 September 2013 flight to conduct a low altitude transect (335 m ± 44 m) across a large section of southern California extending from El Centro, over the Salton Sea, through Banning pass, and finishing near Pasadena (Figure 5; 16:08–16:41 local time). The results show a general reduction of n moving from east (up to 1.54) to west (down to 1.49), which reflects a transition from Background air in the eastern part of the transect to Urban air in the Los Angeles Basin (Figure 5a). Shingler, Crosbie, et al. (2016) previously showed for the same transect that subsaturated aerosol hygroscopicity similarly decreased from east to west, coincident with enhancements in MF$_{OA}$ and reductions in the O:C ratio. More specifically, in the outflow region to the east of the Los Angeles Basin (i.e., east of −117.00°W), considered as Background air, the average MF$_{OA}$ and O:C ratios were 0.61 ± 0.08 and 0.85 ± 0.28,
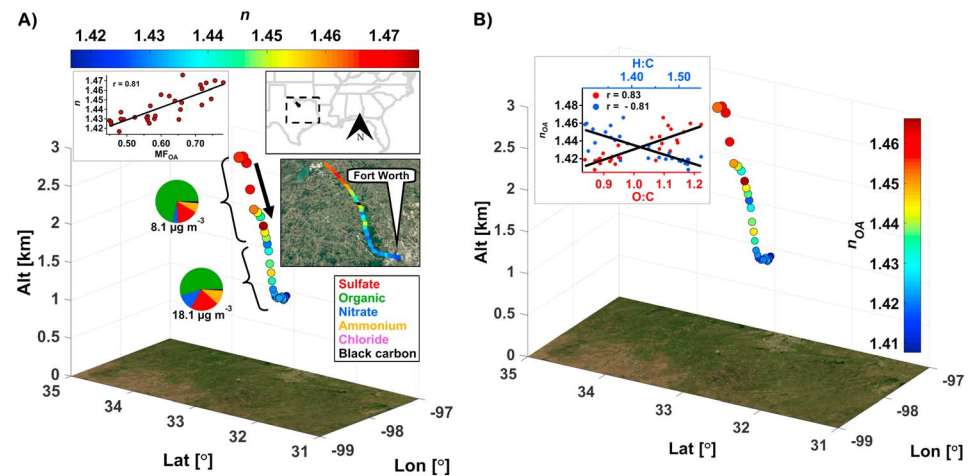
Figure 6. Same as Figure 5 but for a vertical profile (1.04–2.91 km) during a Studies of Emissions and Atmospheric Composition, Clouds and Climate Coupling by Regional Surveys flight on 16 August 2013 (16:26–16:35 local time) near the Texas-Oklahoma border to the west of the Dallas-Fort Worth metropolitan area. Values of $D_{p,dry}$ ranged from 191 to 218 nm. Two air mass types were sampled (Background and Free Troposphere).

respectively. In contrast, the average MF_{OA} and O:C ratios in the Urban area inside the Los Angeles Basin were 0.80 ± 0.01 and 0.53 ± 0.04. There was an inverse relationship between MF_{OA} and n ($r = 0.46$; Figure 5a). Values of n_{OA} during this case study varied from 1.47 to 1.58, with a reduction in value toward the west (Figure 5b). The O:C (H:C) ratio was positively (negatively) related to n_{OA}.

3.2.2. Vertical Structure Over Fort Worth, Texas

On 16 August 2013, the aircraft conducted a downward sounding to the west of the Dallas-Fort Worth metropolitan area in north Texas, with a portion of interest shown between 16:26 and 16:35 (local time) in Figure 6. During the descent from 2.91 to 1.04 km, values of n decreased from as high as 1.48 to as low as 1.42 while sampling, in order, FT and Background air mass types. Similar to the last case, OA comprised the majority of the submicrometer mass concentration; however, unlike the previous case, n was positively correlated with MF_{OA} ($r = 0.81$). The reason for the opposite sign of the relationship between n and MF_{OA} is not obvious but likely is linked to the overall make-up of the rest of the aerosol constituents and the nature of the OA itself. Values of n_{OA} decreased from 1.47 at the higher altitudes to as low as 1.41 at the lower altitudes. Similar to the previous case, n_{OA} was positively (negatively) correlated with the O:C (H:C) ratio.

3.2.3. Vertical Structure Over Houston, Texas

A vertical profile was conducted on the same flight as the last case (16 August 2013; 17:34–17:46 local time) farther south to the west of Houston, Texas (Figure 7). Aspects of this profile were very similar to the one in north Texas, in that n increased with altitude (1.45–1.51 from 1.29 to 4.23 km) as the aircraft sampled the same two air mass types (Background, FT). The submicrometer chemical profile was again dominated by OA, and a strong relationship was observed between n and MF_{OA} ($r = 0.97$). Values of n_{OA} increased from 1.44 at the lower altitudes to as high as 1.49 at the higher altitudes. Similar to the previous two cases, n_{OA} was positively (negatively) correlated with the O:C (H:C) ratio.

3.2.4. Vertical Structure Over Northeastern Wyoming

Two separate cases are examined from a flight on 19 August 2013 over northeastern Wyoming. The first case (12:03–12:36) extended from 0.30 to 2.34 km and was characterized by an increase in n with altitude (1.52–1.57; Figure 8). This case included influence from Background, BB-Wildfire, and Biogenic air masses; consequently, OA was a major component ($MF_{OA} = 0.84 \pm 0.09$). The second case (12:49–13:12) extended between 2.52 and 4.12 km, with a general increase in n with altitude (1.55 to 1.60) (Figure 9). The air mass types examined included FT and BB-Wildfire. Again, the composition was dominated by OA, and this case in particular was the most polluted of all cases with an average submicrometer mass concentration of 43.0 ± 25.7 $\mu g/m^3$.

Values of n and MF_{OA} were positively correlated in both Figures 8a and 9a. Values of n_{OA} increased with altitude in both cases (1.51 to 1.56 in Figure 8b; 1.55–1.60 in Figure 9b). Unlike the other case studies examined,
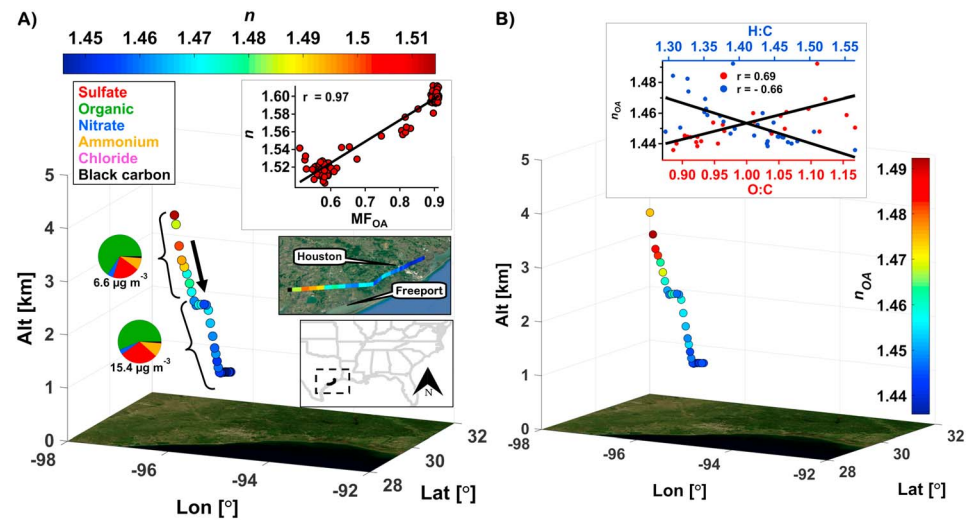
Figure 7. Same as Figure 5 but for a vertical profile (1.29–4.23 km) during a Studies of Emissions and Atmospheric Composition, Clouds and Climate Coupling by Regional Surveys flight on 16 August 2013 (17:34–17:46 local time) over southeast Texas. Values of $D_{p,dry}$ ranged from 204 to 240 nm. Two air mass types were sampled (Background and Free Troposphere). MF_{OA} = mass fraction of organic aerosol.

the two case studies in Figures 8 and 9 exhibited negative (positive) relationships between n_{OA} and the O:C (H:C) ratio. Although the exact reason is unclear with the given data set, important features of these two cases included BB-Wildfire influence and the highest overall MF_{OA} values.

3.2.5. Vertical Structure Over Kinsley, Kansas

The last case examined was from 19 August 2013 (15:22–15:20) when the aircraft examined a column between 0.58 and 3.27 km near Kinsley, Kansas. Values of n increased again with altitude (1.45 to 1.52) during a period where the submicrometer mass was dominated again by OA and the following three air mass types were probed: Background, BB-Wildfire, and FT. Similar to most of the previous cases, n and MF_{OA} were positively correlated. Values of n_{OA} increased with altitude from 1.44 to 1.52, with n_{OA} being positively (negatively) correlated with the O:C (H:C) ratio.

3.2.6. Summary of Case Studies

Significant changes in n were observed in each case study discussed, emphasizing the importance of having high spatial resolution measurements of this important parameter. The overall ranges in n for the six cases varied from as low as 0.05 (Figure 9) to as high as 0.08 (Figure 10). Similarly, derived values of n_{OA} varied between as low as 0.05 (Figure 8) to as high as 0.11 (Figure 5). All cases examining vertical variability (Figures 6–10) revealed that n and n_{OA} increased with altitude, with the common chemical feature being coincident enhancements in MF_{OA} and thus reductions in the contribution of inorganic species. The one case not showing a positive correlation between n and MF_{OA} was from southern California (Figure 5), with a unique feature in that case being that it was characterized by the lowest overall O:C ratio (0.64 ± 0.22). As the O:C ratio was generally positively correlated with n_{OA} (and thus n) in all cases (except when there was BB-Wildfire), systematically lower values in the southern California case may be linked to why n did not reveal a positive correlation with MF_{OA}. The differing correlations in the case studies indicate that trends exist but vary between various types of OA and precursor sources. Future work using a coordinated approach to characterize composition and volatility of OA can help better constrain the relationship between n and SOA composition, as suggested by Moise et al. (2015).

In order to examine how well parametric (i.e., MLR) and nonparametric approaches (i.e., GPR RQK) can predict n, Table 5 summarizes model performance, based on adjusted R^2 values, with predictor variables being MF_{OA}, $MF_{nitrate}$, $MF_{sulfate}$, $MF_{ammonium}$, $MF_{chloride}$, MF_{BC}, and the O:C and H:C ratios of OA. The analysis was done for each case study and the cumulative data set. Mass fractions were used rather than volume fractions to circumvent errors associated with application of the ion pairing technique and assumptions of densities. Furthermore, the use of mass fractions here is meant to be for more practical use based on typical data available from field instruments measuring composition. For the cumulative data set, GPR RQK yielded higher
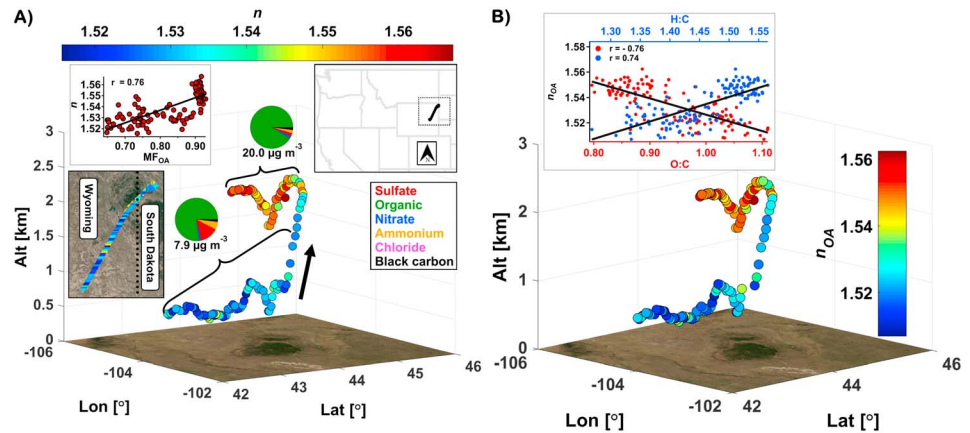
Figure 8. Vertical profile (0.30–2.34 km) during a Studies of Emissions and Atmospheric Composition, Clouds and Climate Coupling by Regional Surveys flight on 19 August 2013 (12:03–12:36 local time) over northeastern Wyoming. Values of $D_{\mathrm{p,dry}}$ ranged from 244 to 267 nm. Three air mass types were sampled (Background, Biomass Burning (BB)-Wildfire, and Biogenic). The arrow signifies the direction of the aircraft. MF_{OA} = mass fraction of organic aerosol.

adjusted R^2 values than MLR, in contrast to most of the individual cases as the latter cases were characterized by a smaller sample size; GPR RQK benefits from having larger sample sets to use for training the model. Unlike the cumulative data set, the results indicate that a linear model can yield fairly good performance in predicting n for simple case studies, with adjusted R^2 values ranging between 0.45 and 0.96. Other work has shown that at least for the organic fraction of aerosol, models relying on quantitative structure-property relationships (Redmond & Thompson, 2011) and group contribution approaches are promising (Cai et al., 2017). However, these methods require information about the aerosol that is difficult to obtain for the complex organic fraction of ambient aerosol with field measurements, such as molecular formula, chemical functionality, and density.

3.3. Sensitivity of AOD and Radiative Forcing to n

To place the variability in n values reported above in perspective, sensitivity calculations were performed for AOD in response to n perturbations between 1.42 and 1.60 for each air mass type. The calculations
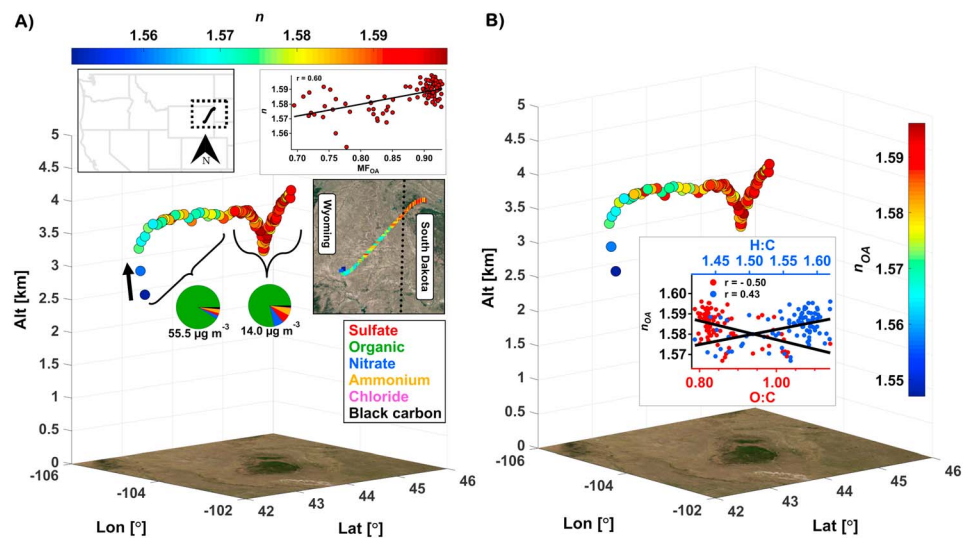

Figure 9. Spatial profile during a Studies of Emissions and Atmospheric Composition, Clouds and Climate Coupling by Regional Surveys flight on 19 August 2013 (12:49–13:12 local time) over northeastern Wyoming. Values of $D_{\mathrm{p,dry}}$ ranged from 271 to 288 nm. Two air mass types were sampled (Biomass Burning (BB)-Wildfire and Free Troposphere). The arrow signifies the direction of the aircraft. MF_{OA} = mass fraction of organic aerosol.
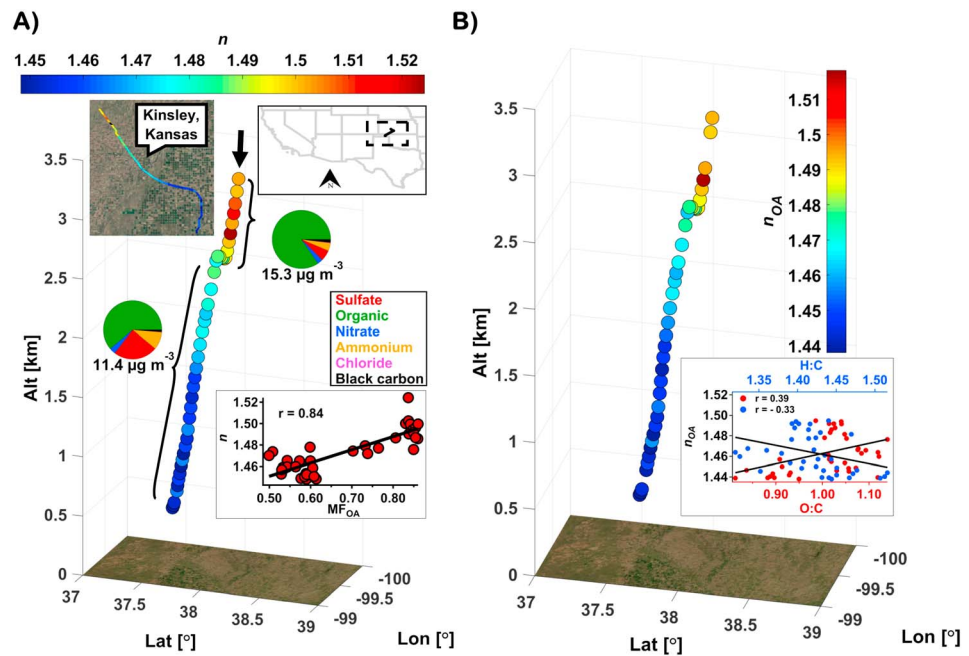
Figure 10. Vertical profile (0.58–3.27 km) during a Studies of Emissions and Atmospheric Composition, Clouds and Climate Coupling by Regional Surveys flight on 19 August 2013 (15:22–15:29 local time) near Kinsley, Kansas. Values of $D_{p,dry}$ ranged from 199 to 228 nm. Three air mass types were sampled (Background, Biomass Burning (BB)-Wildfire, and Free Troposphere). The arrow signifies the direction of the aircraft. MF_{OA} = mass fraction of organic aerosol.

were initialized with the average aerosol size distribution measured for each air mass type in DC3 and SEAC⁴RS using the ultra-high sensitivity aerosol spectrometer for a path length of 2 km, which is a typical planetary boundary layer depth in the sampled areas (Wagner et al., 2015). The sensitivity results are the same with longer path lengths. Calculations were conducted with and without consideration of an imaginary component of 0.05, and they assume spherical particles. Mie calculations relied on the function "Mie_abcd" in MATLAB (Mätzler, 2002). The sensitivity of top of the atmosphere radiative forcing to n perturbations is similar to the sensitivity of AOD for the small values of AOD considered, as shown in other works (Redemann, Turco, Liou, Hobbs, et al., 2000; Thorsen & Fu, 2015). For example, Redemann, Turco, Liou, Hobbs, et al. (2000) showed that a 10% perturbation in AOD resulted in a ~10% error in top of the atmosphere forcing.
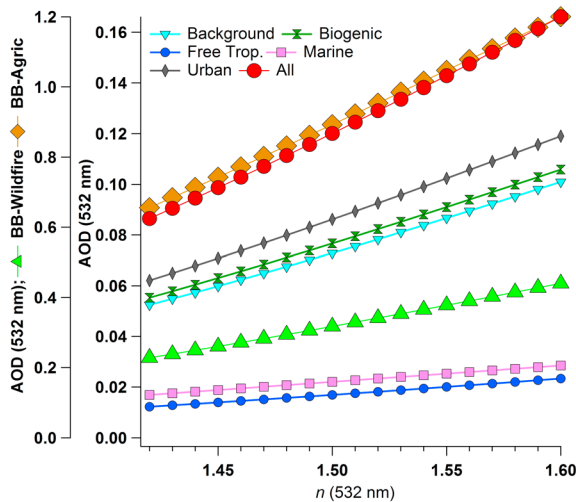
Figure 11 shows an enhancement of AOD as a function of n, with the highest overall values for the two BB categories and the lowest values for the FT and Marine air types. In terms of sensitivity, a perturbation of 0.01 in n results in a change of AOD ranging from 2.3% to 4.7%, depending on the aerosol type and the initial n value. The relative magnitudes of the sensitivities between air mass types (i.e., one type being higher or lower than another type) are preserved when considering a fixed imaginary component of 0.05. Perturbations of 0.05 in n result in AOD changes between 12.9% and 23.8% without an imaginary component and between 11.1% and 18.2% with a 0.05 imaginary component. Finally, the percent change in AOD (and radiative forcing), without assuming an imaginary component, between the minimum and maximum values for each air mass type is as follows in increasing order: 25.0% (BB-Agricultural), 41.9% (Marine), 55.0% (Urban), 88.2% (FT), 89.8% (BB-Wildfire), 92.6% (Background), and 96.8% (Biogenic). These results motivate improved predictive capabilities for this complex aerosol property.

Figure 11. Sensitivity of aerosol optical depth (AOD) to n values using average aerosol size distribution for each air mass type shown for a path length of 2 km, which is representative of the typical planetary boundary layer depth. Note that free troposphere aerosol would be higher in altitude but are treated the same for the purposes of the calculations. Two y axes are used to separate the biomass burning (BB) categories that exhibited much higher AOD values than other air mass types.

While outside the scope of the current work, it is noteworthy to add that the optical sizing instruments are highly sensitive to n values used as part of their algorithms. Using the DASH-SP as just one example, $D_{p,dry}$ can change by nearly a factor of 2 across the range of n values (1.40 to 1.60) typically used in its retrieval algorithm for a representative OPC pulse height distribution (see also Figure 7 of Shingler, Sorooshian, et al., 2016).

4. Conclusions

This study reports a characterization of n using airborne data from the surface level up to 12-km altitude for two field campaigns over North America (DC3 and SEAC⁴RS). The main results of this study include the following:

1. The real part of the refractive index (n), at 532 nm, for dry particles ranged from 1.42 to 1.61 during these campaigns and exhibited mean and median values for the eight defined air mass types between 1.50–1.53 and 1.50–1.54, respectively.
2. Values of n for the OA fraction (n_{OA}) were calculated using a linear mixing rule, with a characteristic value of 1.52 shown to be suitable for n_{OA} when examining the cumulative data set.
3. Case studies showed that n and n_{OA} increased with altitude, simultaneous with MF_{OA} enhancements. Values of n_{OA} were positively (negatively) correlated with the O:C (H:C) ratio in the absence of biomass burning influence.
4. MLR was shown to exhibit decent skill in predicting n based on aerosol chemical data for several case studies. In contrast, GPR was shown to be most effective at predicting n for the cumulative data set.
5. A sensitivity analysis conducted showed that assumptions of constant n values for a single column or for a specific air mass types can lead to a significant error. For example, it was shown that the percent change in AOD (and radiative forcing), without an imaginary component, between the minimum and maximum values for each air mass type ranged from 25.0% (BB-Agricultural) to 96.8% (Biogenic). Previous studies have shown that optical sizing instruments are similarly sensitive to n perturbations.

The results of this study motivate future effort to advance knowledge of the n parameter with the goal of improving its treatment in remote sensing retrievals, modeling, and optical sizing instruments. Furthermore, this study was limited in examining effective n values that include the influence of shape and absorbing materials, and future work would benefit from untangling the effects of those factors in characterization of airborne n data.

References

Abo Riziq, A., Erlick, C., Dinar, E., & Rudich, Y. (2007). Optical properties of absorbing and non-absorbing aerosols retrieved by cavity ring down (CRD) spectroscopy. *Atmospheric Chemistry and Physics*, *7*(6), 1523–1536. https://doi.org/10.5194/acp-7-1523-2007

Anderson, B. E., Grant, W. B., Gregory, G. L., Browell, E. V., Collins, J. E., Sachse, G. W., et al. (1996). Aerosols from biomass burning over the tropical South Atlantic region: Distributions and impacts. *Journal of Geophysical Research*, *101*(D19), 24,117–24,137. https://doi.org/10.1029/96JD00717

Barth, M. C., Cantrell, C. A., Brune, W. H., Rutledge, S. A., Crawford, J. H., Huntrieser, H., et al. (2015). The Deep Convective Clouds and Chemistry (DC3) field campaign. *Bulletin of the American Meteorological Society*, *96*(8), 1281–1309. https://doi.org/10.1175/Bams-D-13-00290.1

Cai, C., Marsh, A., Zhang, Y., & Reid, J. P. (2017). A group contribution approach to predict the refractive index of pure organic components in ambient organic aerosol. *Environmental Science & Technology*, *51*(17), 9683–9690. https://doi.org/10.1021/acs.est.7b01756

Canagaratna, M. R., Jayne, J. T., Jimenez, J. L., Allan, J. D., Alfarra, M. R., Zhang, Q., et al. (2007). Chemical and microphysical characterization of ambient aerosols with the aerodyne aerosol mass spectrometer. *Mass Spectrometry Reviews*, *26*(2), 185–222. https://doi.org/10.1002/mas.20115

Cappa, C. D., Che, D. L., Kessler, S. H., Kroll, J. H., & Wilson, K. R. (2011). Variations in organic aerosol optical and hygroscopic properties upon heterogeneous OH oxidation. *Journal of Geophysical Research*, *116*, D15204. https://doi.org/10.1029/2011JD015918

Chin, M., Ginoux, P., Kinne, S., Torres, O., Holben, B. N., Duncan, B. N., et al. (2002). Tropospheric aerosol optical thickness from the GOCART model and comparisons with satellite and sun photometer measurements. *Journal of the Atmospheric Sciences*, *59*(3), 461–483. https://doi.org/10.1175/1520-0469(2002)059<0461:Taotft>2.0.Co;2

Corr, C. A., Hall, S. R., Ullmann, K., Anderson, B. E., Beyersdorf, A. J., Thornhill, K. L., et al. (2012). Spectral absorption of biomass burning aerosol determined from retrieved single scattering albedo during ARCTAS. *Atmospheric Chemistry and Physics*, *12*(21), 10,505–10,518.

de Gouw, J., & Warneke, C. (2007). Measurements of volatile organic compounds in the Earth's atmosphere using proton-transfer-reaction mass spectrometry. *Mass Spectrometry Reviews*, *26*(2), 223–257. https://doi.org/10.1002/mas.20119

DeCarlo, P. F., Kimmel, J. R., Trimborn, A., Northway, M. J., Jayne, J. T., Aiken, A. C., et al. (2006). Field-deployable, high-resolution, time-of-flight aerosol mass spectrometer. *Analytical Chemistry*, *78*(24), 8281–8289. https://doi.org/10.1021/ac061249n

Dick, W. D., Saxena, P., & McMurry, P. H. (2000). Estimation of water uptake by organic compounds in submicron aerosols measured during the Southeastern Aerosol and Visibility Study. *Journal of Geophysical Research*, *105*(D1), 1471–1479. https://doi.org/10.1029/1999JD901001

Diskin, G. S., Podolske, J. R., Sachse, G. W., & Slate, T. A. (2002). Open-path airborne tunable diode laser hygrometer. In A. Fried (Ed.), *Diode lasers and applications in atmospheric sensing, Proc. Soc. Photo-Optical Instrum. Eng.*, (Vol. 4817, pp. 196–204). https://doi.org/10.1117/12.453736

Dubovik, O., Holben, B., Eck, T. F., Smirnov, A., Kaufman, Y. J., King, M. D., et al. (2002). Variability of absorption and optical properties of key aerosol types observed in worldwide locations. *Journal of the Atmospheric Sciences*, *59*(3), 590–608. https://doi.org/10.1175/1520-0469(2002)059<0590:Voaaop>2.0.Co;2

Ferrare, R. A., Melfi, S. H., Whiteman, D. N., Evans, K. D., Poellot, M., & Kaufman, Y. J. (1998). Raman lidar measurements of aerosol extinction and backscattering—2. Derivation of aerosol real refractive index, single-scattering albedo, and humidification factor using Raman lidar and aircraft size distribution measurements. *Journal of Geophysical Research*, *103*(D16), 19,673–19,689. https://doi.org/10.1029/98JD01647

Flores, J. M., Zhao, D. F., Segev, L., Schlag, P., Kiendler-Scharr, A., Fuchs, H., et al. (2014). Evolution of the complex refractive index in the UV spectral region in ageing secondary organic aerosol. *Atmospheric Chemistry and Physics*, *14*(11), 5793–5806. https://doi.org/10.5194/acp-14-5793-2014

Guyon, P., Boucher, O., Graham, B., Beck, J., Mayol-Bracero, O. L., Roberts, G. C., et al. (2003). Refractive index of aerosol particles over the Amazon tropical forest during LBA-EUSTACH 1999. *Journal of Aerosol Science*, *34*(7), 883–907. https://doi.org/10.1016/S0021-8502(03)00052-1

Gysel, M., Crosier, J., Topping, D. O., Whitehead, J. D., Bower, K. N., Cubison, M. J., et al. (2007). Closure study between chemical composition and hygroscopic growth of aerosol particles during TORCH2. *Atmospheric Chemistry and Physics*, *7*(24), 6131–6144. https://doi.org/10.5194/acp-7-6131-2007

Hameri, K., Laaksonen, A., Vakeva, M., & Suni, T. (2001). Hygroscopic growth of ultrafine sodium chloride particles. *Journal of Geophysical Research*, *106*(D18), 20,749–20,757. https://doi.org/10.1029/2000JD000200

Hand, J. L., & Kreidenweis, S. M. (2002). A new method for retrieving particle refractive index and effective density from aerosol size distribution data. *Aerosol Science and Technology*, *36*(10), 1012–1026. https://doi.org/10.1080/02786820290092276

Haywood, J. M., Roberts, D. L., Slingo, A., Edwards, J. M., & Shine, K. P. (1997). General circulation model calculations of the direct radiative forcing by anthropogenic sulfate and fossil-fuel soot aerosol. *Journal of Climate*, *10*(7), 1562–1577. https://doi.org/10.1175/1520-0442(1997)010<1562:Gcmcot>2.0.Co;2

He, Q. F., Bluvshtein, N., Segev, L., Meidan, D., Flores, J. M., Brown, S. S., et al. (2018). Evolution of the complex refractive index of secondary organic aerosols during atmospheric aging. *Environmental Science & Technology*, *52*(6), 3456–3465. https://doi.org/10.1021/acs.est.7b05742

Hersey, S. P., Craven, J. S., Metcalf, A. R., Lin, J., Lathem, T., Suski, K. J., et al. (2013). Composition and hygroscopicity of the Los Angeles aerosol: CalNex. *Journal of Geophysical Research: Atmospheres*, *118*, 3016–3036. https://doi.org/10.1002/jgrd.50307

Hersey, S. P., Craven, J. S., Schilling, K. A., Metcalf, A. R., Sorooshian, A., Chan, M. N., et al. (2011). The Pasadena Aerosol Characterization Observatory (PACO): Chemical and physical analysis of the western Los Angeles basin aerosol. *Atmospheric Chemistry and Physics*, *11*(15), 7417–7443. https://doi.org/10.5194/acp-11-7417-2011

Hersey, S. P., Sorooshian, A., Murphy, S. M., Flagan, R. C., & Seinfeld, J. H. (2009). Aerosol hygroscopicity in the marine atmosphere: A closure study using high-time-resolution, multiple-RH DASH-SP and size-resolved C-ToF-AMS data. *Atmospheric Chemistry and Physics*, *9*(7), 2543–2554. https://doi.org/10.5194/acp-9-2543-2009

Intergovernmental Panel on Climate Change (2013). Summary for policymakers, in Climate change 2013: The physical science basis. Contribution of Working Group I to the Fifth Assessment Report of the Intergovernmental Panel on Climate Change. In T. F. Stocker, et al. (Eds.) (p. 14). Cambridge, UK: Cambridge University Press.

Kaufman, Y. J., Tanre, D., Remer, L. A., Vermote, E. F., Chu, A., & Holben, B. N. (1997). Operational remote sensing of tropospheric aerosol over land from EOS moderate resolution imaging spectroradiometer. *Journal of Geophysical Research*, *102*(D14), 17,051–17,067. https://doi.org/10.1029/96JD03988

Kim, H., Barkey, B., & Paulson, S. E. (2010). Real refractive indices of alpha- and beta-pinene and toluene secondary organic aerosols generated from ozonolysis and photo-oxidation. *Journal of Geophysical Research*, *115*, D24212. https://doi.org/10.1029/2010JD014549

Kim, H., Barkey, B., & Paulson, S. E. (2012). Real refractive indices and formation yields of secondary organic aerosol generated from photo-oxidation of limonene and alpha-pinene: The effect of the HC/NO$_x$ ratio. *The Journal of Physical Chemistry. A*, *116*(24), 6059–6067. https://doi.org/10.1021/jp301302z

Kim, H., & Paulson, S. E. (2013). Real refractive indices and volatility of secondary organic aerosol generated from photooxidation and ozonolysis of limonene, alpha-pinene and toluene. *Atmospheric Chemistry and Physics*, *13*(15), 7711–7723. https://doi.org/10.5194/acp-13-7711-2013

Kinne, S., Lohmann, U., Feichter, J., Schulz, M., Timmreck, C., Ghan, S., et al. (2003). Monthly averages of aerosol properties: A global comparison among models, satellite data, and AERONET ground data. *Journal of Geophysical Research*, *108*(D20), 4634. https://doi.org/10.1029/2001JD001253

Koepke, P., Hess, M., Schult, I., & Shettle, E. P. (1997). *Global aerosol dataset*, Rep. 243, (p. 44). Hamburg: Max-Plank-Inst. für Meteorol.

Kuwata, M., Zorn, S. R., & Martin, S. T. (2012). Using elemental ratios to predict the density of organic material composed of carbon, hydrogen, and oxygen. *Environmental Science & Technology*, *46*(2), 787–794. https://doi.org/10.1021/es202525q

Lambe, A. T., Cappa, C. D., Massoli, P., Onasch, T. B., Forestieri, S. D., Martin, A. T., et al. (2013). Relationship between oxidation level and optical properties of secondary organic aerosol. *Environmental Science & Technology*, *47*(12), 6349–6357. https://doi.org/10.1021/es401043j

Lenoble, J. (1991). The particulate matter from biomass burning: A tutorial and critical review of its radiative impact. In J. S. Levine (Ed.), *Global biomass burning: Atmospheric, climatic, and biospheric implications* (chap. 46, pp. 381–386). Cambridge, MA: MIT Press.

Levoni, C., Cervino, M., Guzzi, R., & Torricella, F. (1997). Atmospheric aerosol optical properties: A database of radiative characteristics for different components and classes. *Applied Optics*, *36*(30), 8031–8041. https://doi.org/10.1364/Ao.36.008031

Li, J., & Mao, J. T. (1990). Properties of atmospheric aerosols inverted from optical remote-sensing. *Atmospheric Environment: Part A - General Topics*, *24*(9), 2517–2522.

Liu, J. J., Zheng, Y. F., Li, Z. Q., & Wu, R. J. (2008). Ground-based remote sensing of aerosol optical properties in one city in Northwest China. *Atmospheric Research*, *89*(1–2), 194–205. https://doi.org/10.1016/j.atmosres.2008.01.010

Mätzler, C. (2002). MATLAB functions for Mie scattering and absorption, Research Report No. 2002–08, Institute of Applied Physics, University of Bern.

McNaughton, C. S., Clarke, A. D., Howell, S. G., Pinkerton, M., Anderson, B., Thornhill, L., et al. (2007). Results from the DC-8 inlet characterization experiment (DICE): Airborne versus surface sampling of mineral dust and sea salt aerosols. *Aerosol Science and Technology*, *41*(2), 136–159. https://doi.org/10.1080/02786820601118406

Mei, F., Hayes, P. L., Ortega, A., Taylor, J. W., Allan, J. D., Gilman, J., et al. (2013). Droplet activation properties of organic aerosols observed at an urban site during CalNex-LA. *Journal of Geophysical Research: Atmospheres*, *118*, 2903–2917. https://doi.org/10.1002/jgrd.50285

Moise, T., Flores, J. M., & Rudich, Y. (2015). Optical properties of secondary organic aerosols and their changes by chemical processes. *Chemical Reviews*, *115*(10), 4400–4439. https://doi.org/10.1021/cr5005259

Muller, D., Ansmann, A., Wagner, F., Franke, K., & Althausen, D. (2002). European pollution outbreaks during ACE 2: Microphysical particle properties and single-scattering albedo inferred from multiwavelength lidar observations. *Journal of Geophysical Research*, *107*(D15), 4248. https://doi.org/10.1029/2001JD001110

Myhre, G., Stordal, F., Restad, K., & Isaksen, I. S. A. (1998). Estimation of the direct radiative forcing due to sulfate and soot aerosols. *Tellus B*, *50*(5), 463–477. https://doi.org/10.1034/j.1600-0889.1998.t01-4-00005.x

Perring, A. E., Schwarz, J. P., Markovic, M. Z., Fahey, D. W., Jimenez, J. L., Campuzano-Jost, P., et al. (2017). In situ measurements of water uptake by black carbon-containing aerosol in wildfire plumes. *Journal of Geophysical Research: Atmospheres*, *122*, 1086–1097. https://doi.org/10.1002/2016JD025688

Raut, J. C., & Chazette, P. (2008). Vertical profiles of urban aerosol complex refractive index in the frame of ESQUIF airborne measurements. *Atmospheric Chemistry and Physics*, *8*(4), 901–919. https://doi.org/10.5194/acp-8-901-2008

Redemann, J., Turco, R. P., Liou, K. N., Hobbs, P. V., Hartley, W. S., Bergstrom, R. W., et al. (2000). Case studies of the vertical structure of the direct shortwave aerosol radiative forcing during TARFOX. *Journal of Geophysical Research*, *105*(D8), 9971–9979. https://doi.org/10.1029/1999JD901042

Redemann, J., Turco, R. P., Liou, K. N., Russell, P. B., Bergstrom, R. W., Schmid, B., et al. (2000). Retrieving the vertical structure of the effective aerosol complex index of refraction from a combination of aerosol in situ and remote sensing measurements during TARFOX. *Journal of Geophysical Research*, *105*(D8), 9949–9970. https://doi.org/10.1029/1999JD901044

Redmond, H., & Thompson, J. E. (2011). Evaluation of a quantitative structure-property relationship (QSPR) for predicting mid-visible refractive index of secondary organic aerosol (SOA). *Physical Chemistry Chemical Physics*, *13*(15), 6872–6882. https://doi.org/10.1039/c0cp02270e

Reggente, M., Peters, J., Theunis, J., Van Poppel, M., Rademaker, M., De Baets, B., & Kumar, P. (2015). A comparison of strategies for estimation of ultrafine particle number concentrations in urban air pollution monitoring networks. *Environmental Pollution*, *199*, 209–218. https://doi.org/10.1016/j.envpol.2015.01.034

Rogers, S., & Girolami, M. (2016). *A first course in machine learning*. Boca Raton, FL: CRC Press.

Rosati, B., Wehrle, G., Gysel, M., Zieger, P., Baltensperger, U., & Weingartner, E. (2015). The white-light humidified optical particle spectrometer (WHOPS)—A novel airborne system to characterize aerosol hygroscopicity. *Atmospheric Measurement Techniques*, *8*(2), 921–939. https://doi.org/10.5194/amt-8-921-2015

Sachse, G. W., Hill, G. F., Wade, L. O., & Perry, M. G. (1987). Fast-response, high-precision carbon-monoxide sensor using a tunable diode-laser absorption technique. *Journal of Geophysical Research*, *92*(D2), 2071–2081. https://doi.org/10.1029/JD092iD02p02071

Schwarz, J. P., Perring, A. E., Markovic, M. Z., Gao, R. S., Ohata, S., Langridge, J., et al. (2015). Technique and theoretical approach for quantifying the hygroscopicity of black-carbon-containing aerosol using a single particle soot photometer. *Journal of Aerosol Science*, *81*, 110–126. https://doi.org/10.1016/j.jaerosci.2014.11.009

Seinfeld, J. H., & Pandis, S. N. (2016). *Atmospheric chemistry and physics* (3rd ed.). New York: Wiley-Interscience.

Shettle, E. P., & Fenn, R. W. (1979), Models for the aerosol lower atmosphere and the effects of humidity variations on their optical properties, Rep. Tr-79-0214, U.S. Air Force Geophysics Laboratory, Hanscom Air Force Base, Mass.

Shingler, T., Crosbie, E., Ortega, A., Shiraiwa, M., Zuend, A., Beyersdorf, A., et al. (2016). Airborne characterization of subsaturated aerosol hygroscopicity and dry refractive index from the surface to 6.5 km during the SEAC^{4}RS campaign. *Journal of Geophysical Research: Atmospheres*, *121*, 4188–4210. https://doi.org/10.1002/2015JD024498

Shingler, T., Sorooshian, A., Ortega, A., Crosbie, E., Wonaschütz, A., Perring, A. E., et al. (2016). Ambient observations of hygroscopic growth factor and *f*(RH) below 1: Case studies from surface and airborne measurements. *Journal of Geophysical Research: Atmospheres*, *121*, 13,661–13,677. https://doi.org/10.1002/2016JD025471

Sokolik, I. N., & Toon, O. B. (1999). Incorporation of mineralogical composition into models of the radiative properties of mineral aerosol from UV to IR wavelengths. *Journal of Geophysical Research*, *104*(D8), 9423–9444. https://doi.org/10.1029/1998JD200048

Sorooshian, A., Hersey, S., Brechtel, F. J., Corless, A., Flagan, R. C., & Seinfeld, J. H. (2008). Rapid, size-resolved aerosol hygroscopic growth measurements: Differential aerosol sizing and hygroscopicity spectrometer probe (DASH-SP). *Aerosol Science and Technology*, *42*(6), 445–464. https://doi.org/10.1080/02786820802178506

Sorooshian, A., Murphy, S. N., Hersey, S., Gates, H., Padro, L. T., Nenes, A., et al. (2008). Comprehensive airborne characterization of aerosol from a major bovine source. *Atmospheric Chemistry and Physics*, *8*(17), 5489–5520. https://doi.org/10.5194/acp-8-5489-2008

Sorooshian, A., Shingler, T., Crosbie, E., Barth, M. C., Homeyer, C. R., Campuzano-Jost, P., et al. (2017). Contrasting aerosol refractive index and hygroscopicity in the inflow and outflow of deep convective storms: Analysis of airborne data from DC3. *Journal of Geophysical Research: Atmospheres*, *122*, 4565–4577. https://doi.org/10.1002/2017JD026638

Tang, I. N. (1996). Chemical and size effects of hygroscopic aerosols on light scattering coefficients. *Journal of Geophysical Research*, *101*(D14), 19,245–19,250. https://doi.org/10.1029/96JD03003

Taylor, J. R. (1982). *An introduction to error analysis*. Mill Valley, CA: University Science Books.

Thorsen, T. J., & Fu, Q. (2015). CALIPSO-inferred aerosol direct radiative effects: Bias estimates using ground-based Raman lidars. *Journal of Geophysical Research: Atmospheres*, *120*, 12,209–12,220. https://doi.org/10.1002/2015JD024095

Toon, O. B., Maring, H., Dibb, J., Ferrare, R., Jacob, D. J., Jensen, E. J., et al. (2016). Planning, implementation, and scientific goals of the studies of emissions and atmospheric composition, clouds and climate coupling by regional surveys (SEAC(4)RS) field mission. *Journal of Geophysical Research: Atmospheres*, *121*, 4967–5009. https://doi.org/10.1002/2015JD024297

van Beelen, A. J., Roelofs, G. J. H., Hasekamp, O. P., Henzing, J. S., & Rockmann, T. (2014). Estimation of aerosol water and chemical composition from AERONET Sun-sky radiometer measurements at Cabauw, the Netherlands. *Atmospheric Chemistry and Physics*, *14*(12), 5969–5987. https://doi.org/10.5194/acp-14-5969-2014

Wagner, N. L., Brock, C. A., Angevine, W. M., Beyersdorf, A., Campuzano-Jost, P., Day, D., et al. (2015). In situ vertical profiles of aerosol extinction, mass, and composition over the southeast United States during SENEX and SEAC(4)RS: Observations of a modest aerosol enhancement aloft. *Atmospheric Chemistry and Physics*, *15*(12), 7085–7102. https://doi.org/10.5194/acp-15-7085-2015

Wang, C. L., Liu, Y., Everson, R. M., Rahat, A. A. M., & Zheng, S. (2017). Applied Gaussian process in optimizing unburned carbon content in fly ash for boiler combustion. *Mathematical Problems in Engineering*, *2017*, 1–8. https://doi.org/10.1155/2017/6138930

Wang, W., & Rood, M. J. (2008). Real refractive index: Dependence on relative humidity and solute composition with relevancy to atmospheric aerosol particles. *Journal of Geophysical Research*, *113*, D23305. https://doi.org/10.1029/2008JD010165

Westphal, D. L., & Toon, O. B. (1991). Simulations of microphysical, radiative, and dynamic processes in a continental-scale forest-fire smoke plume. *Journal of Geophysical Research*, *96*(D12), 22,379–22,400. https://doi.org/10.1029/91JD01956

Wilson, A., & Adams, R. (2013). Gaussian process kernels for pattern discovery and extrapolation. In Proceedings of the 30th International Conference on Machine Learning (ICML-13, 1067–1075.

Yamasoe, M. A., Kaufman, Y. J., Dubovik, O., Remer, L. A., Holben, B. N., & Artaxo, P. (1998). Retrieval of the real part of the refractive index of smoke particles from Sun/sky measurements during SCAR-B. *Journal of Geophysical Research*, *103*(D24), 31,893–31,902. https://doi.org/10.1029/98JD01211

Zarzana, K. J., Cappa, C. D., & Tolbert, M. A. (2014). Sensitivity of aerosol refractive index retrievals using optical spectroscopy. *Aerosol Science and Technology*, *48*(11), 1133–1144. https://doi.org/10.1080/02786826.2014.963498

Zhang, X. Q., Turpin, B. J., Mcmurry, P. H., Hering, S. V., & Stolzenburg, M. R. (1994). Mie theory evaluation of species contributions to 1990 wintertime visibility reduction in the Grand-Canyon. *Journal of the Air & Waste Management Association*, *44*(2), 153–162. https://doi.org/10.1080/1073161X.1994.10467244